Utilizing In-Orbit CYGNSS Roll Maneuvers for Improved Level-1 Calibration—Part II: Application to Reflected Signal Channels

Mohammad M. Al-Khaldi, *Member, IEEE*, Scott Gleason, *Senior Member, IEEE*, Christopher S. Ruf, *Life Fellow, IEEE*, Joel T. Johnson, *Fellow, IEEE*, Darren S. McKague, *Member, IEEE*, Anthony Russel, William L. Wells, Tianlin Wang, *Senior Member, IEEE*, Dorina Twigg, Patrick McEnaney, and Joshua Synowiec

***Abstract*—This work develops a methodology for using commanded roll maneuvers by Cyclone Global Navigation Satellite System (CYGNSS) constellation observatories to improve the determination of the nadir antenna patterns that receive GNSS signals reflected from Earth's surface. The method relies on observation geometry properties in differing roll states that are used as a diagnostic tool to reveal Level-1 calibration errors associated with prelaunch mischaracterization of the nadir antenna patterns and as numerical constraints on algorithms to derive improved patterns that are more representative of in-orbit gain levels. It is shown that the updated gain estimates differ by −3 to 3 dB in a nonuniform fashion. In the companion work (Part III), the effects the use of these updated patterns has in terms of advancing the consistency of the calibration quality of observables is explored. Initial assessments presented here highlight how observable anomalies attributable to inconsistencies in the characterization of in-orbit nadir may be reduced by over 50% using the proposed methodologies.**

***Index Terms*—Cyclone Global Navigation Satellite System (CYGNSS), global navigation satellite systems reflectometry (GNSS-R), GPS effective isotropic radiated power (EIRP), Level-1 calibration, microwave remote sensing, normalized bistatic radar cross section (NBRCS).**

Received 9 November 2025; revised 21 February 2026 and 29 April 2026; accepted 18 May 2026. Date of publication 21 May 2026; date of current version 29 May 2026. This work was supported by the National Aeronautics and Space Administration (NASA) Science Mission Directorate through the University of Michigan under Contract NNL13AQ00C. The work of Tianlin Wang was supported by the Jet Propulsion Laboratory, California Institute of Technology, through the National Aeronautics and Space Administration under Grant 80NM0018D0004. *(Corresponding author: Mohammad M. Al-Khaldi.)*

Mohammad M. Al-Khaldi and Joel T. Johnson are with the Department of Electrical and Computer Engineering and the ElectroScience Laboratory, The Ohio State University, Columbus, OH 43210 USA (e-mail: al-khaldi.2@osu.edu).

Scott Gleason is with Daaxa LLC, Boulder, CO 80307 USA.

Christopher S. Ruf and Darren S. McKague are with the Department of Climate and Space Sciences and Engineering, University of Michigan, Ann Arbor, MI 48109 USA.

Anthony Russel is with Muon Space, Mountain View, CA 94043 USA.

William L. Wells is with the Southwest Research Institute, San Antonio, TX 78238 USA.

Tianlin Wang is with the NASA Jet Propulsion Laboratory, California Institute of Technology, Pasadena, CA 91109 USA.

Dorina Twigg, Patrick McEnaney, and Joshua Synowiec are with the Space Physics Research Laboratory, University of Michigan, Ann Arbor, MI 48109 USA.

Digital Object Identifier 10.1109/TGRS.2026.3695341

I. Introduction

THE operation of the Cyclone Global Navigation Satellite System (CYGNSS) mission's eight satellite constellation [1] as passive, specular, bistatic radar systems provides advantages compared to other Earth remote sensing systems in terms of platform cost, revisit characteristics, and robustness of observables. However, CYGNSS's reliance on ±1 MHz coarse acquisition (C/A) codes originating from independent GPS transmitters, each with distinct signal properties and whose reflections can be received in any part of the receivers' nadir azimuthal and elevation antenna patterns, gives rise to multiple calibration challenges. Refinement of the mission's Level-1 (L1) calibration practices, therefore, continues to be a subject of ongoing investigation.

While multiple spaceborne global navigation satellite systems reflectometry (GNSS-R) L1 calibration methods have been previously reported [2], [3], [4], [5], [6], [7], [8], [9], this work considers a new approach that leverages constraints placed on receive antenna gain patterns that result from CYGNSS satellite observations in different attitude ("roll") states. CYGNSS satellite roll maneuvers serve both as a diagnostic tool, enabling the identification of calibration anomalies, and as part of an algorithm to improve characterization of in-orbit nadir antenna patterns. While CYGNSS roll maneuvers were initially intended to maintain power budgets by maximizing solar panel exposure to sunlight when needed (see Part I [10] for a complete overview), they also give rise to unique measurement properties relating to the observation geometry that underpin the procedures explored here.

A summary of CYGNSS's normalized bistatic radar cross section (NBRCS) and reflectivity observables is provided in Section II, followed by an overview of the new calibration methodologies in Section III. This section addresses how rolled data is used to identify discrepancies between prelaunch and in-orbit nadir antenna patterns and also presents the method used to independently derive nadir antenna patterns across 16 channels (eight satellites, each having port and starboard antennas). The updated antenna patterns obtained are then compared to prelaunch patterns in Section IV. The impact of the updated zenith antenna patterns, GPS transmit gain patterns (see Part I [10]), and nadir antenna patterns on

1558-0644 © 2026 IEEE. All rights reserved, including rights for text and data mining, and training of artificial intelligence and similar technologies. Personal use is permitted, but republication/redistribution requires IEEE permission.
See https://www.ieee.org/publications/rights/index.html for more information.

Authorized licensed use limited to: University of Michigan Library. Downloaded on July 22,2026 at 17:42:47 UTC from IEEE Xplore. Restrictions apply.

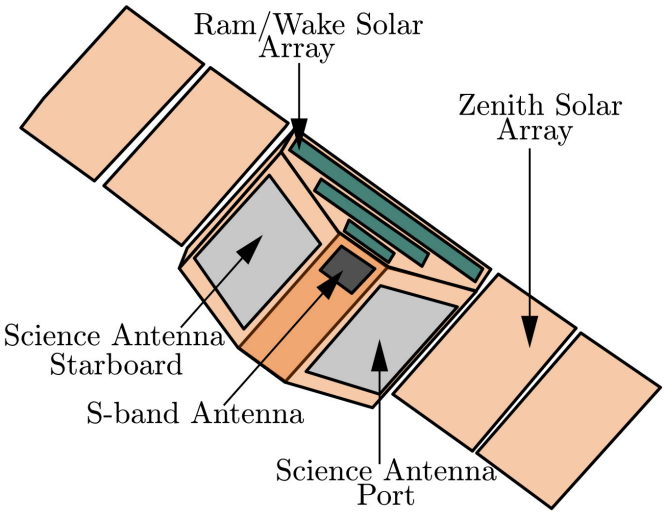


Fig. 1. Bottom view of CYGNSS spacecraft.

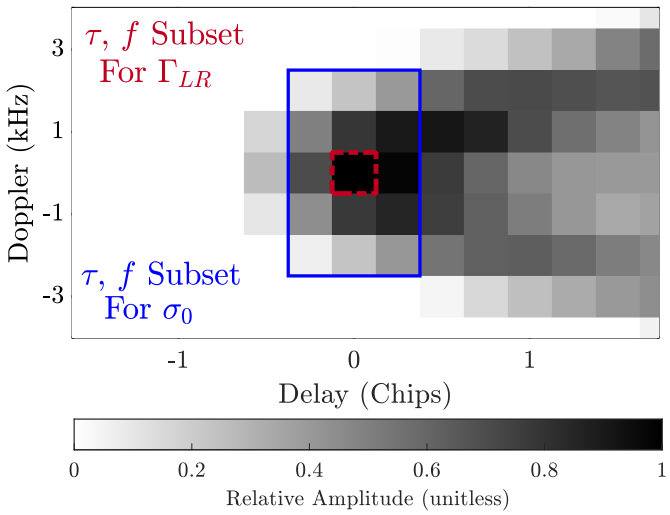


Fig. 2. Illustrative example of a standard CYGNSS Level-1 DDM highlighting the delay τ Doppler f spaces over which the constellation's two primary observables, NBRCS σ_0 and surface reflectivity Γ_{LR}, are computed.

observables' consistency is also briefly discussed but explored in further detail in a companion work (see Part III [11]). This is complemented with a discussion of several practical considerations in Section V, followed by final conclusions and discussions in Section VI.

While representative examples are shown using observations made by specific CYGNSS receivers to illustrate the utility of the proposed methodologies, the reported trends generalize across all receivers and transmitters. Analysis of the properties of CYGNSS's observations across varied roll maneuvers also shows that they present numerous avenues for improving the calibration of GNSS-R systems. The techniques presented here, therefore, constitute only an example of a wider range of approaches for incorporating in-orbit roll maneuvers as part of GNSS-R system calibration.

II. Background

During CYGNSS's routine GNSS-R operations, each of seven receivers (eight prior to the failure of FM06 in November 2022) monitors four tracks of specularly reflected signals originating from GPS transmissions. The reflections can be tracked by either of two "port" and "starboard" nadir antennas. An illustration of a CYGNSS flight model is depicted in Fig. 1. The two antennas are separate, side-looking modules with the starboard antenna oriented along the $\phi^N = 90°$ azimuth direction while the port antenna is oriented along the $\phi^N = 270°$ azimuth direction; the receiver's velocity vector is along $\phi^N = 0°$. The reflections are then correlated with corresponding "clean" local C/A code replicas to form an onboard "full DDM" (delay Doppler map) spanning 128 delay pixels (sampled at $\approx$ 0.25 chips) and 20 Doppler pixels (sampled at 500 Hz) [12]. Over a measurement's 0.5-s integration period (1 s prior to August 2019), 500 1 ms coherently integrated DDMs are incoherently averaged, giving rise to the nominal 2-Hz Level-1 data rate. An onboard cropping and compression algorithm selects a smaller 17 $\times$ 11 delay/Doppler subset centered about the full DDM's peak for storage and downlinking. The smaller subset is the Level-1 DDM, an example of which is depicted in Fig. 2. The downlinked DDMs are initially produced in uncalibrated "raw counts" and subsequently undergo the calibration procedure

$$\sigma^0 = \frac{(4\pi)^3}{\lambda^2} \cdot \left(\frac{P_B + P_r}{C_B \cdot (1 - c_N (1 - \Lambda(b)))} \right) \cdot \left(\frac{R_T^2 R_R^2 L_a}{E^{Z,S} \cdot G^{R,N}} \right) \cdot \frac{\sum_{i=-1}^{1} \sum_{j=-2}^{2} C(\tau_T + i, f_T + j) - C_N}{\sum_{i=-1}^{1} \sum_{j=-2}^{2} \overline{A}(\tau_T + i, f_T + j)} \quad (1)$$

for NBRCS σ^0 and

$$\Gamma_{LR} = \frac{(4\pi)^2}{\lambda^2} \cdot \left(\frac{P_B + P_r}{C_B \cdot (1 - c_N (1 - \Lambda(b)))} \right) \cdot \left(\frac{(R_T + R_R)^2 L_a}{E^{Z,S} \cdot G^{R,N}} \right) \cdot * arg\, max_{\tau^*, f^*} (C(\tau, f) - C_N) \quad (2)$$

and surface reflectivity Γ_{LR}. A summary of Level-1 calibration terms used to derive primary observables from CYGNSS's uncalibrated raw count DDMs is included in Table I. The term $\Lambda(b)$ is a function [6] intended to compensate for discretization artifacts associated with CYGNSS's 2-bit analog-to-digital converters (ADCs) with the channel-specific scale factors c_N listed in Table II.

Previous studies have used σ^0 and various derived products in the sensing of oceanic properties, including wind

TABLE I
Summary of Level-1 Calibration Terms Used to Derive Primary Observables From CYGNSS's Uncalibrated Raw Count DDMs

Term	Definition	Term	Definition
λ	Wavelength	P_B	Black body thermal noise level
C_B	Black body counts	P_r	Receiver thermal noise level
L_a	Atmospheric loss	R_T	Range, GPS to specular point
$G^{R,N}$	Antenna gain	R_R	Range, specular point to CYGNSS
C	DDM in counts	$E^{Z,S}$	Effective isotropic radiated power
C_N	Noise floor	$\overline{A}$	Effective scattering area DDM
τ_T	Specular bin τ index	f_T	Specular bin f index
c_N	Scale factor	Λ	Digital sampling correction

Authorized licensed use limited to: University of Michigan Library. Downloaded on July 22,2026 at 17:42:47 UTC from IEEE Xplore. Restrictions apply.

TABLE II
CHANNEL SPECIFIC INSTRUMENT c_N SCALING FACTORS

FM→	1	2	3	4	5	6	7	8
Star	-1.59	-1.40	-1.79	-1.49	-2.19	-1.60	-1.60	-1.79
Port	-1.49	-1.49	-1.39	-1.40	-1.49	-1.79	-1.99	-1.80

speed [13], [14], convective activity [15], [16], heat fluxes [17], [18], and the Madden–Julian oscillation (MJO) [19], [20], while Γ_{LR} over land has been used in studies of soil freeze/thaw dynamics [21], [22], moisture [23], [24], [25], [26], inundation [27], [28], [29], vegetation biomass [30], [31], [32], and methane emissions [33], [34].

Any errors in the calibration terms in (1) and (2) have the potential to compromise the observables' relationship to the geophysical properties of interest. Al-Khaldi et al. [10] address the use of in-orbit CYGNSS roll maneuvers for improving zenith antenna pattern characterization. Section III explores the means with which the properties of "rolled measurements" can be leveraged for improving nadir antenna pattern characterization. Emphasis is initially placed on the use of σ^0 estimates over the ocean because land measurements experience more complex scattering phenomena [35], [36] and are impacted by the confounding effects of vegetation, roughness, moisture, and inland water bodies. The impact of the updated patterns on the calibration quality of Γ_{LR} is nonetheless also later explored in [11].

III. PROPOSED METHODOLOGY

Simulations or prelaunch anechoic chamber measurements of antenna patterns are typically applied in GNSS-R calibration, but such prelaunch-only methods can be inaccurate.

An illustration of the inconsistency in prior calibration of the NBRCS of the ocean surface, and of the improvement in consistency that results from the revised calibration presented here, is shown in Fig. 3. The figure plots the mean difference between the NBRCS observed when the spacecraft is rolled and when it is not rolled as a percentage of the value when it is not rolled. This "NBRCS anomaly" is defined as

$$\tilde{\sigma}_0(\theta_i, \varphi_r) = \frac{\frac{100}{N_r}\sum_{i=1}^{N_r}\sigma^0(\theta_i, \varphi_r) - \frac{100}{N_0}\sum_{i=1}^{N_0}\sigma^0(\theta_i, 0)}{\frac{1}{N_0}\sum_{i=1}^{N_0}\sigma^0(\theta_i, 0)} \quad (3)$$

where θ_i is the incidence angle, φ_r is the roll angle, N_r is the number of rolled observations averaged, and N_c is the number of nonrolled observations averaged. Observations are only included for which the wind speed at the ocean surface was between 6 and 8 m/s, as determined by European Centre for Medium Range Weather Forecasts Reanalysis v5 (ERA5) data product. While ERA5 reanalysis data do not represent "ground truth" for surface properties at the time of observation and are subject to uncertainty, the estimates they provide are an adequate reference source for the purposes of this study. Four separate estimates of $\tilde{\sigma}^0$ are shown in Fig. 3, one pair when the spacecraft is rolled by $-10°$ and $+10°$ using the initial patterns and a second pair at the same two roll angles using the updated patterns. The actual NBRCS of the ocean surface

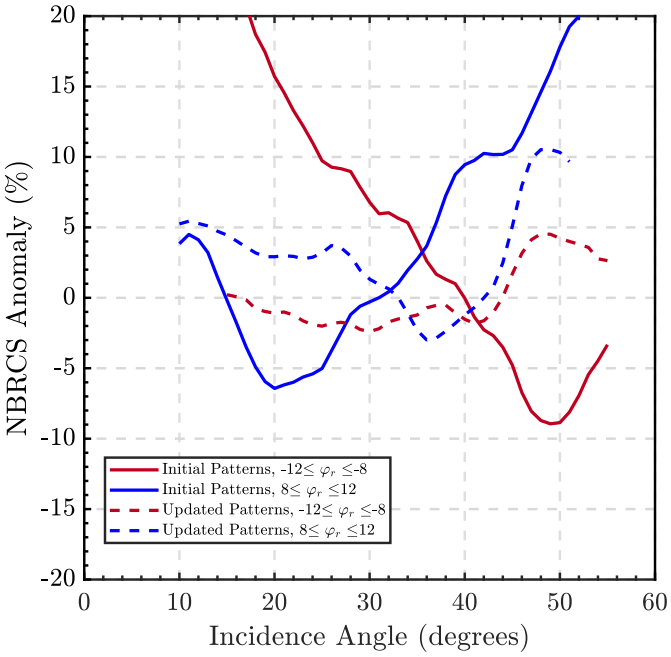


Fig. 3. FM01, Starboard NBRCS anomalies for observations with $6 \le u_{10} \le 8$ m/s ERA5 wind speeds at roll angles $\varphi_r = +10°$ and $\varphi_r = -10°$. View is limited to the range of incidence angles over which 90% of the measurements exist. Initial patterns refer to estimates of the nadir antenna patterns primarily informed by mock-up chamber measurements using flight module replicas and publicly available characterizations of the GPS antenna patterns.

can vary as a function of incidence angle, but it does not vary as a function of spacecraft roll angle, so it should be the same at $\varphi_r = -10°$, $0°$, or $+10°$. In other words, a perfect calibration algorithm would produce $\tilde{\sigma}^0$ of zero at all incidence angles. In Fig. 3, $\tilde{\sigma}^0$ levels using initial patterns are seen to vary by as much as 20%, and their dependence on incidence angle changes between the two roll states in a systematic and antisymmetric way. The $\tilde{\sigma}^0$ levels using the revised calibration, while still not perfect, are seen to be significantly reduced both in magnitude and in their dependence on roll state.

The strong dependence of the $\tilde{\sigma}^0$ utilizing the initial patterns on roll state suggests that the root cause of its calibration problem is likely due to an error in the assumed gain pattern of the receive antenna. To explore this, consider how the antenna gain in the direction of a fixed point on the Earth's surface will change as the spacecraft's roll angle changes. Because the antenna is rigidly mounted to the spacecraft, it will also roll, and its gain in a particular direction will vary according to the shape of the antenna pattern. The calibration algorithm attempts to correct for the antenna gain, but does so accurately only if the gain pattern is correct. The $\tilde{\sigma}^0$ is evaluated with respect to incidence angle in Fig. 3 in order to highlight this relationship, since the angle of incidence of a GNSS-R measurement is determined by the location of the receive antenna but is independent of its attitude.

Next, to further explore the dependence these observed trends have on calibration uncertainties, Fig. 4 illustrates azimuth and elevation locations in the starboard nadir antenna pattern that map to "mainlobe" Earth incidence angle $25° \le \theta_i \le 26°$ across the three roll states using the mission's complete data record. While the azimuth space ϕ^N of each

Authorized licensed use limited to: University of Michigan Library. Downloaded on July 22,2026 at 17:42:47 UTC from IEEE Xplore. Restrictions apply.

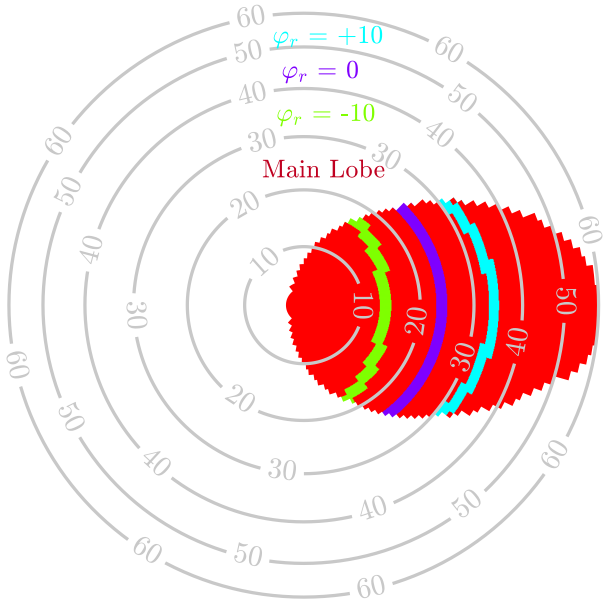


Fig. 4. Illustration of geometry periodicities across different roll angles. Locations in polar co-ordinates of FM01-starboard measurements whose incidence angles fall in the range $25° \leq \theta_i \leq 26°$ for measurements collected using FM01-starboard roll angles of $\varphi_r = 0$, +10, and −10.

roll state is similar, measurements occur at distinct elevation angle co-ordinates θ^N. For example, at $\varphi_r = 0$, antenna pattern locations $25° \leq \theta^N \leq 26°$ consistently occur, while $\varphi_r = +10$ results in $15° \leq \theta^N \leq 16°$ and $\varphi_r = -10$ corresponds to $35° \leq \theta^N \leq 36°$. Together, Figs. 3 and 4 suggest antenna pattern uncertainties can be important. For a fixed Earth incidence angle, measurements in the different roll states occur in distinct portions of the nadir antenna pattern so that pattern errors over a wide angle space can cause significant calibration errors.

While Figs. 3 and 4 highlight the usefulness of in-orbit roll maneuvers as a diagnostic tool; they can also be used to improve the calibration of L1 observables by deriving nadir antenna patterns that may be more representative of in-orbit levels. The means for doing so are described in what follows.

A. Incidence Angle Dependence

The procedures described in [10] and in this work seek to ensure that measurements do not exhibit anomalous dependencies on specific observation geometries, roll states, or GPS transmitters, and that they consistently map to known geophysical properties irrespective of said dependencies. Al-Khaldi et al. [10] used rolled data to improve characterizations of dynamically measured transmitter effective isotropic radiated powers (EIRPs). The approach was premised on the desire to realize a zenith calibration chain that ensures that measured transmit powers associated with each GPS SVN are constant, and a reference P_T was assumed as part of the procedure's initial steps. For a given transmitter SVN, the expectation of a constant P_T is justified in part by the utilization of data where the transmitters are known to not have been operated in a "flex power" mode (i.e., transmitted power levels were constant for each of the SVNs) and the fact that, while measured EIRPs will be "shaped" by the transmitters' gain patterns across different off-boresight angles θ^B, the corresponding P_T should exhibit no dependence on observation geometry. For more details, see [10].

A similar procedure applies for nadir observations, where, after controlling for surface conditions, nadir patterns are derived in a manner that ensures consistent magnitudes irrespective of roll state, antenna pattern co-ordinates, and other calibration parameters. NBRCS calibration, however, is complicated by the fact that σ^0 is expected to depend on both surface wind speeds and incidence angles. The latter can vary from $0° \leq \theta_i \leq 60°$ in GNSS-R observations. Two ocean scenes with identical geophysical properties observed at two different incidence angles can then differ by an amount that depends on the difference between observation angles $\theta_{i,1}$ and $\theta_{i,2}$. It is thus of interest to standardize measurements made at different incidence angles to a common angle using

$$\sigma^c = \frac{\sigma^0}{f(\theta_i)} \tag{4}$$

where σ^c is an incidence angle independent NBRCS. As in [42], measurements are referenced to nadir $\theta_i = 0°$ in what follows. Two approaches, model or empirical, may be used to specify the normalizing function $f(\theta_i)$.

The model approach is based on the formulation for the NBRCS of an ocean-like surface presented in [37]. Model predictions are based on the physical optics approximation (equivalent to the first-order small-slope approximation for specular scattering) for specular scattering from a Gaussian random process surface. The model numerically evaluates the complete Kirchhoff integral for surface scattering, so that the geometrical optics approximation for specular scattering is not required for surfaces of low to moderate roughness in terms of the electromagnetic wavelength. Because the Kirchhoff integral can be challenging to evaluate numerically, the integration approaches described in [38] are applied to ensure accurate evaluations. The ocean-like surfaces considered are described in terms of their power spectral density function, taken to be that of Elfouhaily et al. [38], Hwang et al. [39], [40], or an isotropic Pierson–Moskowitz spectrum [41]. The power spectral density functions of these models are parametrized by the wind speed at 10-m height above the surface and by other parameters such as inverse wave age and water depth; predictions were generated for fully developed seas and for infinite water depth. For each of these sea surface descriptions, the specular NBRCS was computed as a function of wind speed and incidence angle, with $f(\theta_i)$ then determined using (4). The dependence on angle predicted by the model can be interpreted as arising from the slight decrease in the surface reflectivity as incidence angle increases, combined with an increase in the NBRCS in most cases due to an apparent reduction in surface slope variance as the incidence angle increases.

To empirically estimate $f(\theta_i)$, recall that Fig. 4 shows that a fixed Earth incidence angle can occur in distinct antenna pattern locations depending on the roll state. Similarly, measurements made in the three roll states considered map to distinct incidence angle ranges. For example, Fig. 5 shows that

Authorized licensed use limited to: University of Michigan Library. Downloaded on July 22,2026 at 17:42:47 UTC from IEEE Xplore. Restrictions apply.

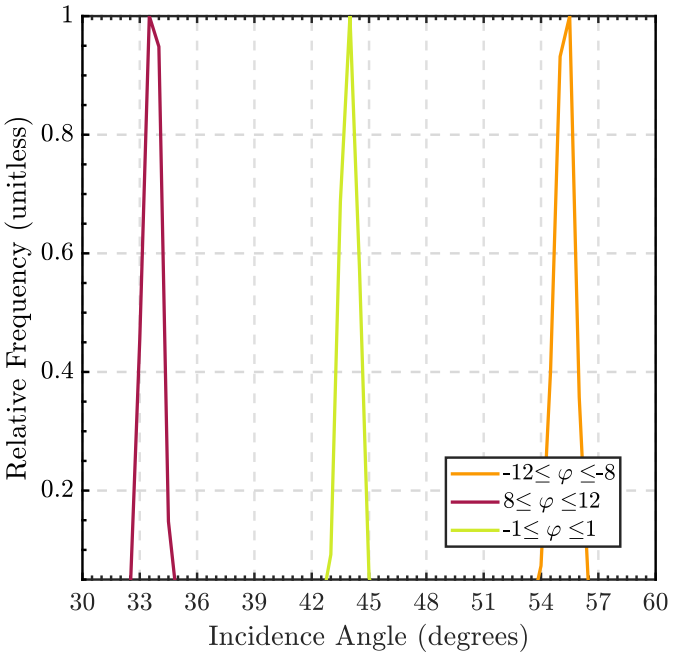


Fig. 5. Illustration of geometry periodicities across different roll angles, highlighting reciprocal relationship associated with incidence angle distributions and nadir antenna polar locations using the example of FM01-starboard measurement densities. Trends are for antenna pattern pixel circumscribed by the limits $43° \le \theta^N \le 45°$ and $74° \le \phi^N \le 76°$.

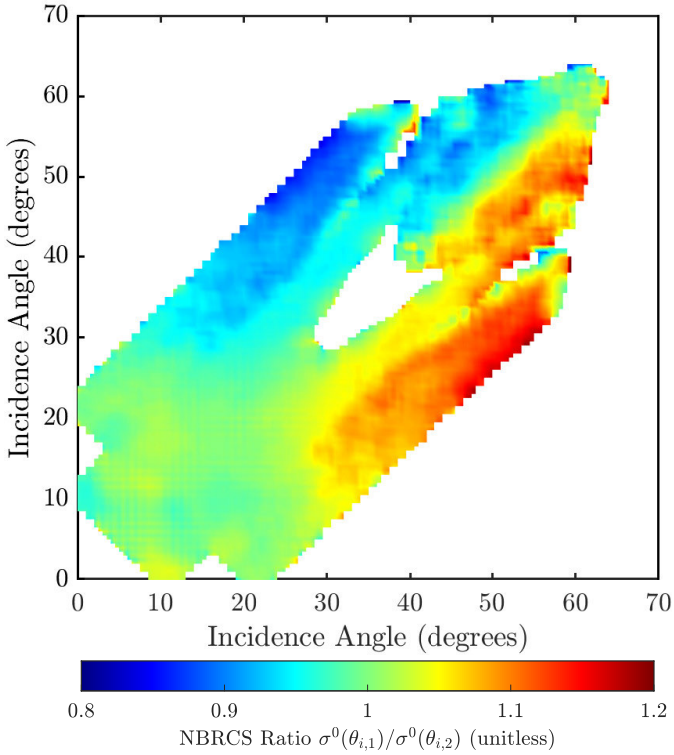


Fig. 6. Empirically derived incidence angle dependence trends. The matrix $\Re(\theta_i, \theta_i)$ communicates the ratio of NBRCS whose incidence angle is indicated by the x-axis value relative to an NBRCS measured at an incidence angle whose value is indicated by the y-axis.

antenna pattern locations $43° \le \theta^N \le 45°$ and $74° \le \phi^N \le 76°$ occur almost exclusively at $\theta_i = 44°$, $34°$, and $54°$ for roll angles $\varphi_r = 0°$, $+10°$, and $-10°$, respectively. It follows that at that particular antenna pattern "pixel" (i.e., θ_N and ϕ_N combination) the ratios $\sigma^0_{-10}/\sigma^0_0 \approx f(\theta_i = 54)/f(\theta_i = 44)$, $\sigma^0_{-10}/\sigma^0_{+10} \approx f(\theta_i = 54)/f(\theta_i = 34)$, and $\sigma^0_0/\sigma^0_{+10} \approx f(\theta_i = 44)/f(\theta_i = 34)$ may be computed. These ratios provide estimates of the empirical relationship that relates observations made at $\theta_i = 54°$ to those made at $\theta_i = 44°$ as well as $\theta_i = 33°$, in addition to the $\theta_i = 44°$ to $\theta_i = 34°$ relationship. Because these ratios are computed at fixed antenna polar co-ordinates based on the observation geometries, they are independent of any antenna pattern errors, given that at a fixed θ^N and ϕ^N any $G^{R,N}$ is common and would be canceled by the ratio computed. The capacity to do so is enabled by the availability of data in the various rolled states, as obtaining estimates at multiple incidence angles would otherwise necessitate sampling multiple locations of the antenna pattern, thereby limiting the capacity to decouple the incidence angle dependence and antenna gain level uncertainty.

As the antenna pattern space is traversed across all 16 nadir antenna patterns, other combinations are formed, thereby allowing for the construction of a more complete "ratio matrix" $\Re(\theta_i, \theta_i)$ as depicted in Fig. 6. Several features are noteworthy, including the empirical estimates of ≈ 1 along the one-to-one line as expected. The symmetry of the matrix is also evident as information is mirrored about the 1-1 line; for example the ratio of observations at $f(\theta_i = 50)/f(\theta_i = 30) \approx 1.25$ from below the 1-1 line is equivalent to the ratio $f(\theta_i = 30)/f(\theta_i = 50) \approx 0.8$ above the 1-1 line. A complication arises in regions where no ratios are reported. This includes, for example, the lack of any ratios relating $\theta_i = 60°$ observations with any whose incidence angle is below $\theta_i = 32°$. This is because the matrix $\Re(\theta_i, \theta_i)$ is constructed using data at the two roll angles + 10 and −10 and the incidence angle offsets they give rise to relative to measurements made at $\varphi_r = 0°$. The capacity to furnish larger offsets to relate a wider range of angle pairs may be expanded by roll maneuvers at more extreme angles. This, however, may be an impractical solution as rolls as large as 50° would be needed to reduce the $\theta_i = 32°$ cutoff to $\theta_i = 15°$; such rolls are appreciably greater than the desired capacity for referencing measurements to nadir and therefore estimating the ratio $f(\theta_i = 60°)/f(\theta_i = 0°)$. Instead, a closer inspection of the Fig. 6 matrix makes clear that "effective ratios" may be computed using the available combinations. For example, the series for the following equation can be computed:

$$\begin{aligned} f(60) &\approx \Re(60, 50) \cdot \Re(50, 30) \cdot \Re(30, 10) \cdot \Re(10, 0) \\ &\approx \frac{\sigma^0(60)}{\sigma^0(50)} \cdot \frac{\sigma^0(50)}{\sigma^0(30)} \cdot \frac{\sigma^0(30)}{\sigma^0(10)} \cdot \frac{\sigma^0(10)}{\sigma^0(0)} \\ &\approx \frac{\sigma^0(60)}{\sigma^0(0)}. \end{aligned} \tag{5}$$

In which the required terms are available and, since the terms corresponding to observations at $\theta_i = 50°$, $30°$, and $10°$ all cancel, the desired "effective ratio" is obtained. The same process is applied across all incidence angles and all combinations, with the resulting empirical curve depicted in Fig. 7.

Authorized licensed use limited to: University of Michigan Library. Downloaded on July 22,2026 at 17:42:47 UTC from IEEE Xplore. Restrictions apply.

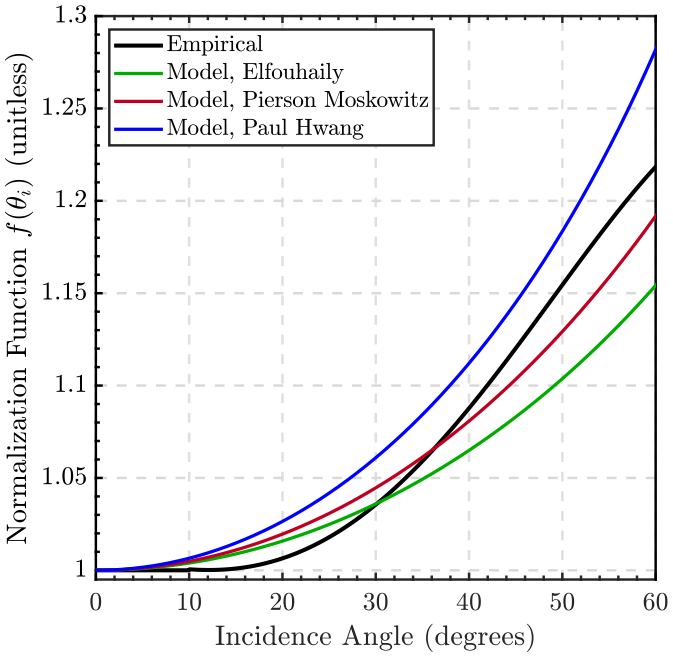


Fig. 7. Comparisons of model based and empirical $f(\theta_i)$ functions developed using measurements in the $6 \le u_{10} \le 8$ (m/s) wind speed range.

Both the modeled and empirical results concur that an increase in NBRCS as a function of incidence angle, relative to $\theta_i = 0°$ observations, should be expected. For measurements made at $\theta_i \le 10°$, both the model predictions and the empirical $f(\theta_i)$ suggest negligible variability, while relative NBRCS changes exceeding 20% are obtained for $\theta_i \ge 50°$. Comparisons across all predictions suggest a peak difference contributing no more than 0.5 dB, and the use of any of the curves can provide an adequate normalization for the continued studies of this article. Because the analysis summarized in Figs. 6 and 7 represents a first attempt at empirically reconstructing NBRCS incidence angle behaviors in a manner thought to be independent of any antenna gain uncertainties; more analysis prior to the adoption of these empirical functions was deemed necessary. Therefore, in what follows, the model-informed $f(\theta_i)$ is used for the normalization process. Future investigators exploring these empirical relationships under roll, particularly over other more complex land scenes, are of interest, as the form of the empirical function may provide information on surface properties and scattering mechanisms. Given the use of Elfouhaily's spectrum in support of CYGNSS's other calibration and validation activities [43], [44], the corresponding $f(\theta_i)$ from Fig. 7 is used in what follows, and can be approximated using:

$$f(\theta_i) = \alpha_1 \theta_i^3 + \alpha_2 \theta_i^2 + \alpha_3 \theta_i + \alpha_4 \tag{6}$$

where $\alpha_1 = 2.303 \times 10^{-7}$, $\alpha_2 = 2.522 \times 10^{-5}$, $\alpha_3 = 2.569 \times 10^{-4}$, and $\alpha_4 = 0.999$.

B. Gain Solutions

Next, it is desirable to identify the range of nadir antenna gains that would ensure that reported NBRCS estimates are identical for the three roll states to a prescribed margin (ρ^{ref}) of a reference NBRCS value σ^{ref}, i.e.,

$$\left| \frac{\sigma_0^c G^{R,N,p}\left(\theta^N, \phi^N\right)}{G_0^{R,N}\left(\theta^N, \phi^N\right)} - \sigma^{ref} \right| \le \rho^{ref} \sigma^{ref} \tag{7}$$

$$\left| \frac{\sigma_{+10}^c G^{R,N,p}\left(\theta^N, \phi^N\right)}{G_{+10}^{R,N}\left(\theta^N, \phi^N\right)} - \sigma^{ref} \right| \le \rho^{ref} \sigma^{ref} \tag{8}$$

$$\left| \frac{\sigma_{-10}^c G^{R,N,p}\left(\theta^N, \phi^N\right)}{G_{-10}^{R,N}\left(\theta^N, \phi^N\right)} - \sigma^{ref} \right| \le \rho^{ref} \sigma^{ref}. \tag{9}$$

Here, the angle-normalized NBRCS products σ_r^c at roll angle r are scaled using the ratio of the initial pattern $G^{R,N,p}(\theta^N, \phi^N)$ used as part of the L1 calibration process (1) to the desired "true" antenna pattern of that roll state $G_r^{R,N}$. The process is repeated across all 16 antennas and every polar pixel defined by the coordinates θ^N and ϕ^N. Overly restrictive ρ^{ref} margins were found to limit the capacity to derive antenna gain solutions across the full polar spaces of the 16 nadir channels, while overly permissive thresholds would not adequately address the desire to ensure NBRCS consistency. A $\rho^{ref} = 10\%$ was found adequate. Equations (7)–(9) can be combined to seek a consistent pattern across all three roll states; the only physical set of antenna gain solutions is that falls within the region of intersection of all three sets as follows:

$$G^{N,R} = G_0^{R,N} \cap G_{+10}^{R,N} \cap G_{-10}^{R,N}. \tag{10}$$

The subset of antenna gain solutions in $G^{N,R}$ all meet the $\rho^{ref} = 10\%$ requirement, and an optimal final gain solution $G_f^{N,R}$ is designated the value that minimizes the overall difference relative to σ^{ref} across all three roll states

$$*arg\,min_{G_f^{N,R*}(\theta^N,\phi^N)} \sum_{r=1}^{3} \left| \frac{\sigma_r^c G^{R,N,p}\left(\theta^N, \phi^N\right)}{G_f^{R,N}\left(\theta^N, \phi^N\right)} - \sigma^{ref} \right| \tag{11}$$

where the subscript r denotes a prescribed roll state. The development of σ^{ref} is informed by several practical considerations. The subset of NBRCS measurements used should be limited to surface conditions where it is reasonable to assume that a quasi-constant NBRCS should be measured. As a result, the measurements used were limited to those over ocean surfaces having reference surface wind speeds within a prescribed range. A measurement density sufficient to fill the patterns' complete polar spaces is also required. Scenes with high wind speeds have the potential to complicate this process due to power saturation effects and loss of sensitivity. Conversely, measurements made over ocean surfaces with lower wind speeds may give rise to coherent or mixed scattering effects for which the NBRCS may be sensitive to the presence of nonlocally generated waves [35]. Informed by these considerations, measurements having ERA5 wind speeds $6 \le u_{10} \le 8$ m/s were used. The reference σ^{ref} value was based on the mean of the measurements falling within the polar space circumscribed by $23° \le \theta^N \le 27°$ and $87° \le \phi^N \le 93°$ on starboard channels and $267° \le \phi^N \le 273°$ on port channels. Each of CYGNSS's nadir antennas is side-looking with boresights centered about $\theta^N = 25°$ and $\phi^N = 90°$ for the starboard antenna and $\theta^N = 25°$ and $\phi^N = 270°$ for the port antenna.

Authorized licensed use limited to: University of Michigan Library. Downloaded on July 22,2026 at 17:42:47 UTC from IEEE Xplore. Restrictions apply.

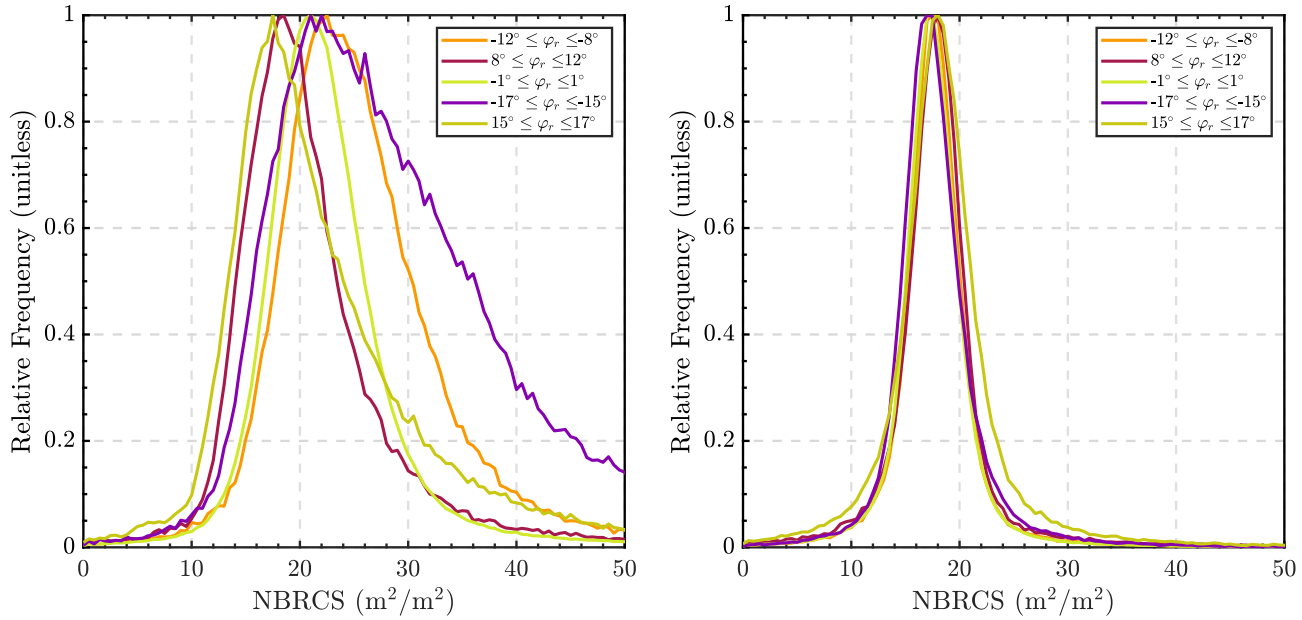


Fig. 8. Initial illustration of the impact of utilizing updated antenna patterns on NBRCS consistency statistics across different roll angles. This exclusively comprises measurements, both in terms of roll angles and reference wind speed ranges, that were not used as part of the process of deriving the updated patterns. The wind speed range is $12 \leq u_{10} \leq 15$ m/s. (a) Using initial pattern characterizations. (b) Using updated patterns thought to be more representative of in-orbit levels.

Irrespective of the peak gain levels (approximately 15 dBi), the choice of this particular polar space to develop the σ^{ref} value is motivated by the expectation that pattern uncertainty is reduced in this angle space. The resulting reference value, normalized for incidence angles using the function $f(\theta_i)$ in the wind speed range $6 \leq u_{10} \leq 8$ m/s, is 21.94 m^2/m^2.

Other than this reference value, the process to obtain the 16 nadir patterns is decoupled from any prelaunch or initial characterizations of the nadir antenna patterns. The procedure constructs antenna patterns that ensure NBRCS consistency across the three roll states considered and over the wind speed range $6 \leq u_{10} \leq 8$ m/s that should be more representative of true, in-orbit gain levels. Fig. 8 provides an initial assessment of performance using NBRCS statistics in the wind speed range $12 \leq u_{10} \leq 15$ m/s. Given FM01's higher power draw, a need arises to roll the receiver to larger roll angles so that Fig. 8 also includes estimates from $\varphi_r = 16°$ and $\varphi_r = -16°$. Both in terms of surface winds and roll angles, this subset of measurements was not utilized in the process of deriving the gain patterns. Across all roll states, NBRCS estimates for the corrected patterns (right plot) are found to be nearly independent of roll state. In contrast, errors in the prelaunch estimates give rise to significant variations with roll state (left plot), including a spread in the modes of the roll angle-specific probability density functions (PDFs). Prelaunch patterns result in a spread of 1.26 dB, whereas the spread is reduced to 0.23 dBs using the updated patterns. In addition, PDFs with the updated patterns maintain a similar Weibull distribution whose standard deviation is limited to 4.73 (m^2/m^2). PDF shape distortions and an NBRCS standard deviation as high as 8.80 (m^2/m^2) occur without pattern correction. A more comprehensive assessment of the impacts of the updated patterns is explored in Section IV.

After obtaining initial pattern estimates on a polar grid having resolutions $\Delta\theta^N = 0.1°$ and $\Delta\phi^N = 0.2°$, several filtering and smoothing procedures are applied. Particular emphasis is placed on retaining the original pattern structure while concurrently capturing and rectifying local anomalies and various other discontinuities. A modified median-absolute deviation filter (also known as a Hampel filter [45]) was applied using the following equation, where detections are made if the condition:

$$\left| G_f^{N,R}\left(\theta^N, \phi^N\right) - \Upsilon\left(\tilde{G}\right) \right| > \frac{-1}{\sqrt{2}Q\left(3/2\right)} \Upsilon\left(\left|\tilde{G} - \Upsilon\left(\tilde{G}\right)\right|\right) \quad (12)$$

is met. Υ is the median operator and Q is the inverse complementary error function. This algorithm is applied recursively over windows as large as 2° and as fine as 0.2° in both azimuth and elevation, with the corresponding gain pattern entries contained in the matrix $\tilde{G}$, to identify and exclude "global" and "local" anomalies. In conjunction, any resulting gaps are filled via nearest-neighbor bilinear interpolation. A moving median smoothing filter is also applied over windows as large as 3° and as fine as 0.2°. An example of the effect of this process is depicted in Fig. 9, contrasting a prescreened gain solution cut with the final curve. The overall structure and amplitude of the gain levels are retained while addressing the local discontinuities that appear at $\theta^N = 30°$, 47°, 50°, 53°, and 54° in an automated fashion. In this case, it is also noted that a modest augmentation of gain levels in the pattern's "null" at $\theta^N = 37°$ increases gain predictions from −10.5 to −9 dB. As almost no measurements fall in these polar spaces, such effects have been found to have a negligible impact on aggregate statistics [11].

Authorized licensed use limited to: University of Michigan Library. Downloaded on July 22,2026 at 17:42:47 UTC from IEEE Xplore. Restrictions apply.

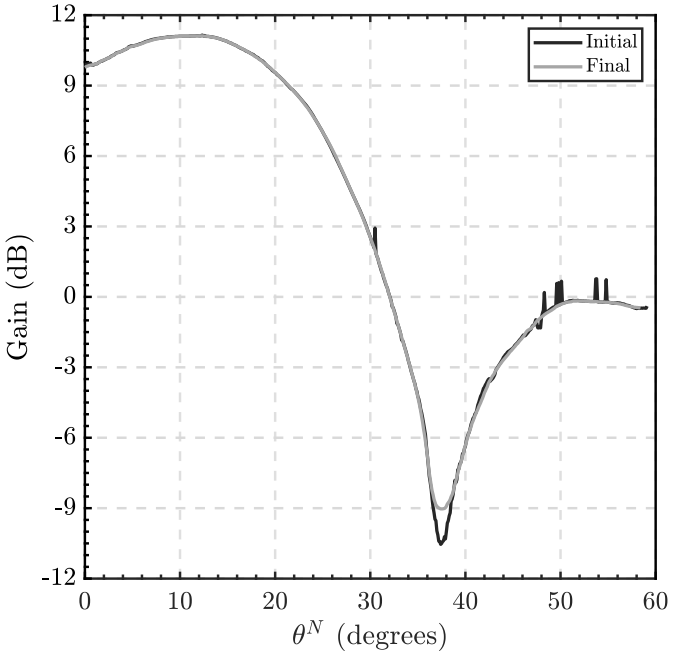


Fig. 9. Example gain cut highlighting the effects of the filtering and smoothing procedure applied.

IV. Resulting Antenna Gain Patterns

Example initial, updated, and difference nadir antenna gain patterns for selected starboard and port channels are depicted in Figs. 10 and 11, respectively. An initial comparison makes clear that the proposed process gives rise to antenna gain distributions that are both realistic and consistent with the general trends of high versus low gains suggested by the initial antenna patterns. In all cases, peak gains are on the order of 15 dB with some interchannel variability. For example, peak in-orbit FM01-starboard gains in Fig. 10(d) are 15.70 dB while the initial patterns in Fig. 10(a) has 15.06 dB. Conversely, a slight reduction is suggested by the updated patterns for FM08-starboard in Fig. 10(c) and (f), where in-orbit gains are thought to be closer to 14.26 dB, 0.57 dB lower than the original estimates. Similar peak gain levels, with a comparable level of variability, are noted across the port-side channels in Fig. 11.

The updated patterns also indicate slightly modified half-power beamwidths (HPBWs) compared to prelaunch estimates in Fig. 10(a)–(c) on the starboard side and their port-side counterparts in Fig. 11. For example, the prelaunch patterns suggest azimuth HPBW$_\phi$ of 57° and depression HPBW$_\theta$ of 32.70°, whereas the updated patterns indicate HPBW$_\phi$ of 58° and depression HPBW$_\theta$ of 36.00° for the FM01 starboard antenna. As a result of the broader HPBW$_\theta$, a higher percentage of measurements are recorded with greater "true" gain levels than the corresponding prelaunch pattern suggests. Importantly, the nonuniformity of the gain differences between prelaunch and updated gain patterns depicted in subplots Fig. 10(g)–(i) is emphasized. For example, on FM01's starboard antenna differences ranging between 0 and 2.5 dB are suggested in Fig. 10(g). Similar nonuniform variability is also noted in the patterns' sidelobes. In the case of FM01-starboard, the updated patterns suggest that gains in the sidelobes are consistently higher than prelaunch estimates and peak at 1.95 dB. Similar trends are also noted for FM03 and FM08 difference patterns in Fig. 10(h) and (i) where an underestimation of gain levels by up to 2.5 dB and an overestimation by up to 0.75 dB, depending on the exact polar co-ordinates within the sidelobes, can occur. Closer to nadir, prelaunch estimates are found to be representative of in-orbit levels with a difference < 0.5 dB relative to the updated patterns, while a significant portion of the antennas' mainlobes appear to overestimate gain levels by varying margins. For FM03, the updated gain estimates are 0.5 dB lower at the antenna's boresights, peaking at 14.74 dB, and can be up to 1 dB lower at the polar co-ordinates $\theta^N = 40°$, $\phi^N = 100°$. For FM08, the updated patterns suggest that gains can be up to 2.5 dB lower than previously thought, in the vicinity of the same polar co-ordinates. Similar complex, nonuniform variability of gain is noted on the port side in Fig. 11(g)–(i) emphasizing the need for the pixel-wise implementation of the operations described in Section III. This also suggests that simpler operations applying constant "debiasing" terms for every receiver channel as a means of ensuring observables' magnitude consistency across all 16 channels are likely to be of limited efficacy.

Comparisons of Figs. 10 and 11 also highlight the fact that using the proposed procedure, two sidelobes occur for the starboard channels while only one sidelobe results for the port channels. The inability to derive a secondary sidelobe on port-side channels relates to the lack of specular reflection tracks in the respective polar coordinates. The CYGNSS on-board observation allocation algorithm uses a pair of uploadable antenna gain maps. These maps are coarse, low-resolution representations of the CYGNSS port and starboard nadir antenna gain patterns (5° steps in θ^N and 15° steps in ϕ^N) that aid in the ranking of potential specularly reflected signals tracked, and prioritize those predicted to have higher quality. Notably, these maps include only the port and starboard main lobes, with the side lobes set to a fill value. This was done intentionally to force prioritization of the reflections in the higher gain main beams. An artifact of this design is that surface reflections located in the side-lobes are only allocated to one of the four available tracking channels if there are fewer than four valid reflections in the two main beams. In cases when there are fewer than four main beam observations, the instrument will not idle the remaining channels and instead allocates these channels to additional reflections. While the details of the allocation algorithm are proprietary, the results suggest that the starboard antennas' sidelobes are first considered, followed by one of the two port-side sidelobes.

With respect to the effects this has on observables, Fig. 3, which showed the impact of nadir antenna pattern mischaracterizations on roll-specific NBRCS anomalies, also shows the benefits of the updated patterns. Significant improvements are noted where the anomalies exhibit a reduced dependence on incidence angle, typically less than 5%. Any residual calibration uncertainties can still contribute to anomalies that can reach up to 12% in a smaller subset of incidence angles. As later shown in Part III [11], the impact this has on other figures of merit appears minimal.

Authorized licensed use limited to: University of Michigan Library. Downloaded on July 22,2026 at 17:42:47 UTC from IEEE Xplore. Restrictions apply.

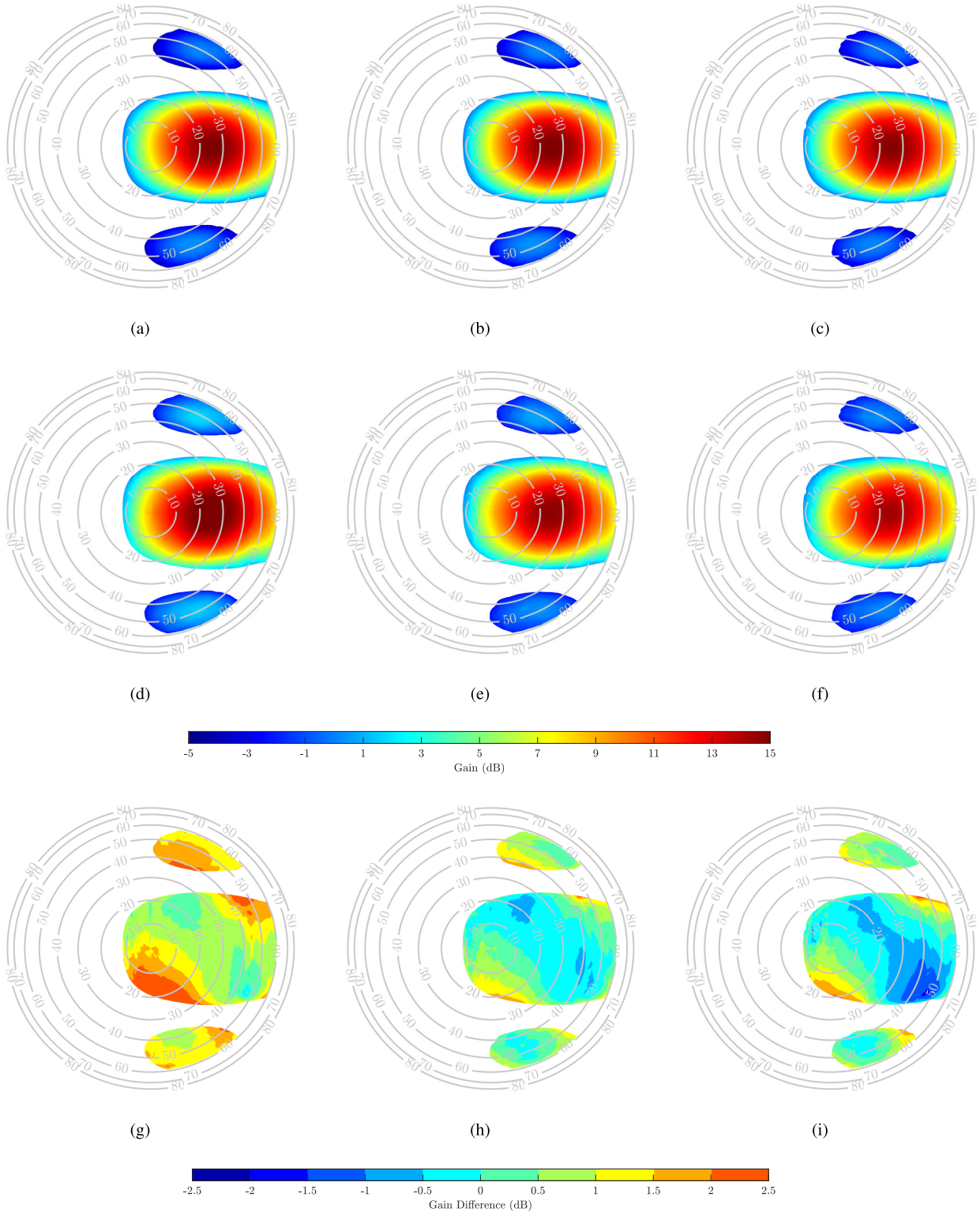


Fig. 10. Comparisons of example nadir starboard gain patterns. Reported difference patterns computed as $G_{updated} - G_{existing}$. (a) Gain, Prelaunch—FM01. (b) Gain, Prelaunch—FM03. (c) Gain, Prelaunch—FM08. (d) Gain, Updated—FM01. (e) Gain, Updated—FM03. (f) Gain, Updated—FM08. (g) Gain Difference—FM01. (h) Gain Difference—FM03. (i) Gain Difference—FM08.

V. Practical Considerations

A. Roll States

The operations (7)–(9) leading to updated nadir gain patterns, as well as those relating to the zenith channel parameters in [10], can be generalized to a larger number of roll angles. A sufficient measurement density across a varied and greater number of roll angles is expected to place further constraints on gain solutions, thereby further improving the process of reconstructing patterns. Nonetheless, operators of future GNSS-R instruments may be limited in terms of the number of roll angles they may be able to maneuver their flight

Authorized licensed use limited to: University of Michigan Library. Downloaded on July 22,2026 at 17:42:47 UTC from IEEE Xplore. Restrictions apply.

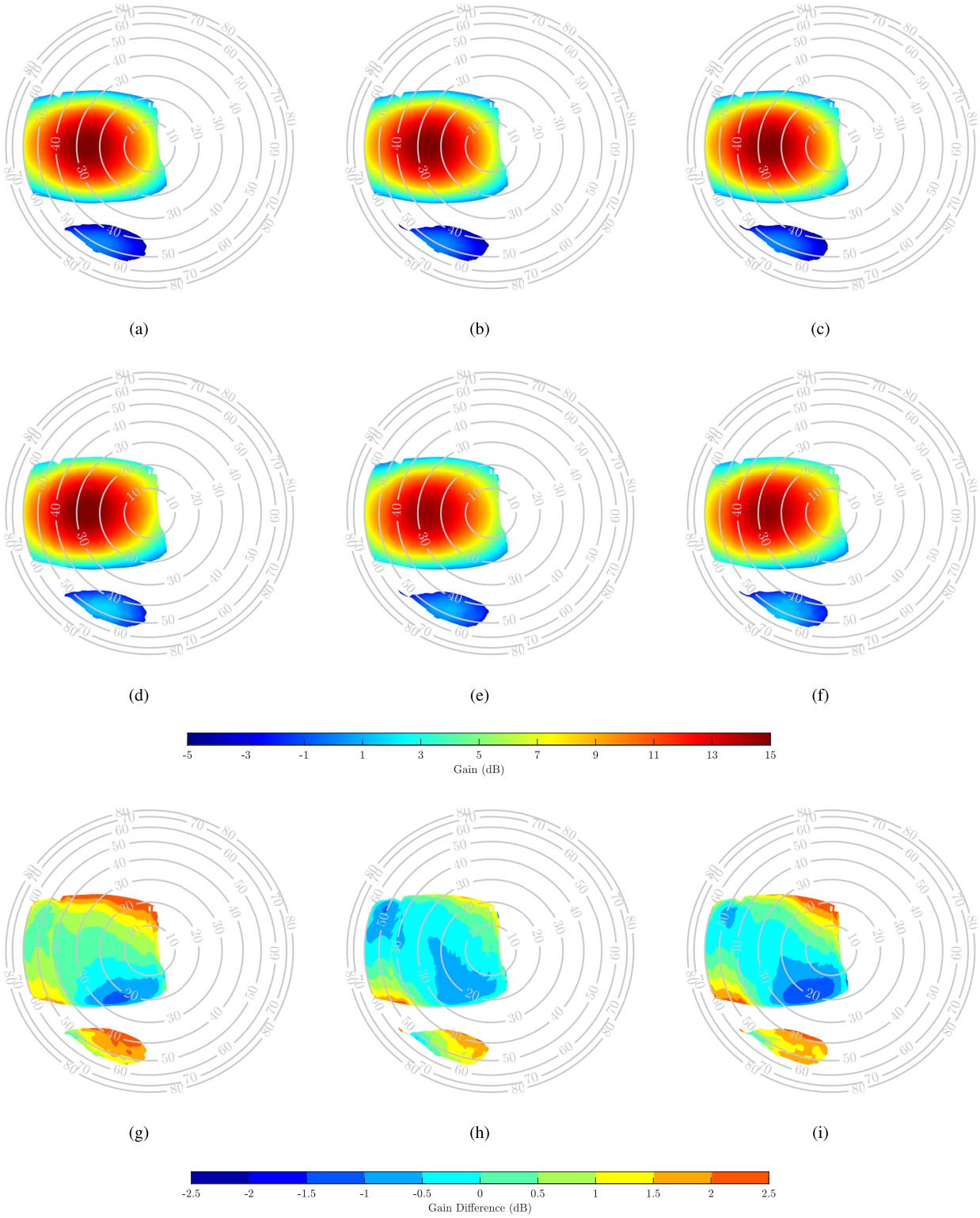


Fig. 11. Comparisons of example nadir port gain patterns. Reported difference patterns computed as $G_{updated} - G_{existing}$. (a) Gain, Prelaunch—FM01. (b) Gain, Prelaunch—FM03. (c) Gain, Prelaunch—FM08. (d) Gain, Updated—FM01. (e) Gain, Updated—FM03. (f) Gain, Updated—FM08. (g) Gain Difference—FM01. (h) Gain Difference—FM03. (i) Gain Difference—FM08.

models into due to mechanical constraints or due to other considerations relating to the interruptions this may cause to their routine science operations. As such, it is of interest to explore the minimum number of roll angles needed to pursue the prescribed procedures. While the operations described in (7)–(9) can be be pursued at two roll angles, nonrolled (i.e., $\varphi_r = 0°$) and an additional ($\varphi_r \neq 0°$) state, the minimum number of roll angles required for a given antenna is thought to be three. To elucidate this, measurement densities on an example starboard antenna across the three roll angles

Authorized licensed use limited to: University of Michigan Library. Downloaded on July 22,2026 at 17:42:47 UTC from IEEE Xplore. Restrictions apply.

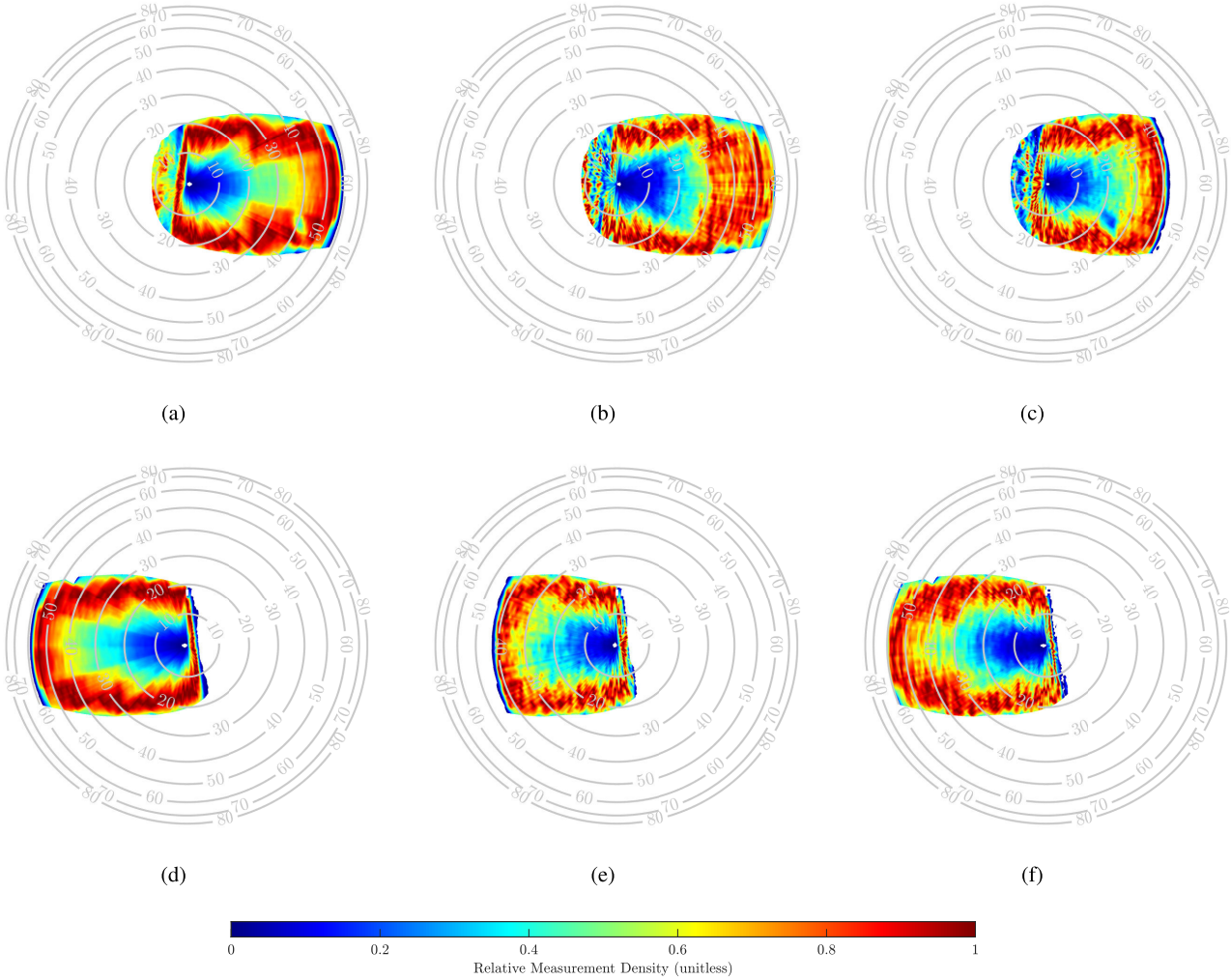


Fig. 12. Relative measurement densities projected on nadir antenna patterns across different roll states using example FM05 observations. (a) Star, $\varphi_r = 0°$. (b) Star, $\varphi_r = +10°$. (c) Star, $\varphi_r = -10°$. (d) Port, $\varphi_r = 0°$. (e) Port, $\varphi_r = +10°$. (f) Port, $\varphi_r = -10°$.

$\varphi_r = 0°, +10°$, and $-10°$ are depicted in Fig. 12. At $\varphi_r = -10°$, few measurements occur beyond $\theta^N = 40°$ such that in the corresponding polar space it is the pair of σ^c_{+10} and σ^c_0 NBRCS estimates that will primarily enable the derivation of updated gain estimates. Conversely, for $\varphi_r = +10°$, relatively fewer measurements occur at angles less than $\theta^N = 20°$ such that in the corresponding polar space, it is the pair of σ^c_{-10} and σ^c_0 NBRCS estimates that will primarily enable the derivation of updated gain estimates. In both cases, this is due to periodicities in how observation geometries map to the antennas' polar space at the different roll angles. A similar, but polarity-flipped, trend applies to all port antennas. As such, and given the need to reliably derive gains across the antennas' complete respective polar spaces, a minimum of three collections at three roll angles is thought to be required. The magnitude of the rolls required will depend on the specific properties of the antenna module(s) utilized and their orientation.

B. Measurement Density

Closely related is the consideration of the number of measurements required to derive reliable and repeatable gain solutions. In the work described in the preceding sections, the ocean NBRCS estimates whose reference ERA5 winds fell within the range $6 \leq u_{10} \leq 8$ m/s measured at roll angles $\varphi_r = 0°$, $+10°$, and $-10°$ used a data record extending from March 2020 to August 2025, furnishing tens of thousands of measurements per pixel. The impact of the updated patterns was later tested using data recorded starting August 2019, using ocean measurements across all reported wind speeds, as well as land measurements, both taken at all roll angles, the majority of which did not play a role in or inform the process leading to updated antenna patterns. Nonetheless, it is acknowledged that future GNSS-R measurements may have interest in applying this method using a more limited data record of measurements and therefore a lower measurement density per-pixel. It is therefore of interest to assess the impact of reduced measurement density on gain solutions. This is assessed via a Monte Carlo study in which the volume of data used is reduced by factors of 50%, 25%, and 10%. The choice of data is randomized across ten trials per reduction factor, and for each trial, the resulting gain patterns are compared (differenced) to the original results, which were shown in Figs. 10 and 11. The mean difference per reduction factor is depicted in Fig. 13, where it is observed that, irrespective of

Authorized licensed use limited to: University of Michigan Library. Downloaded on July 22,2026 at 17:42:47 UTC from IEEE Xplore. Restrictions apply.

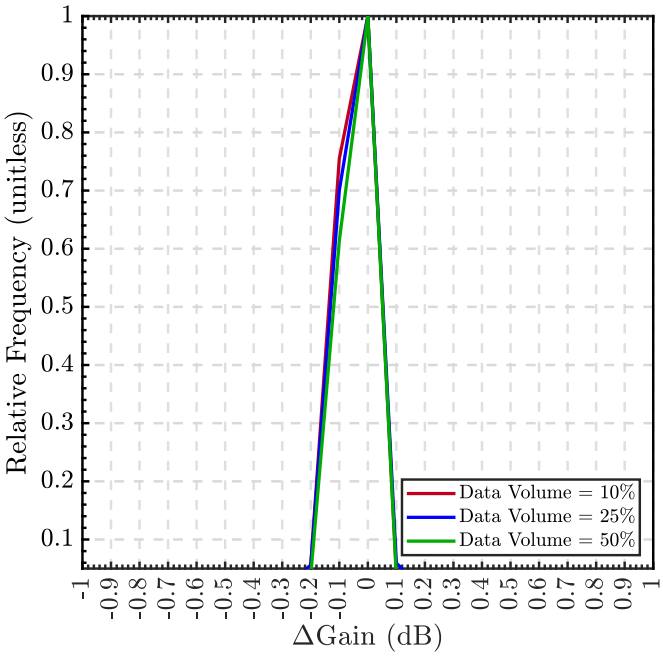


Fig. 13. Gain difference pdf capturing trends from all 16 nadir antenna patterns as part of a Monte Carlo study intended to assess the impact of reducing measurement density used as part of the process of developing nadir antenna patterns.

the reduction factor, peak differences on average are limited to 0.2 dB. Furthermore, analysis suggests that a minimum of 100 measurements for every roll angle at a given polar pixel would be sufficient for deriving similar results (with a comparable difference margin) to those previously reported.

VI. Conclusion

This work demonstrates the utility of in-orbit roll maneuvers both as a diagnostic tool intended to identify potential mischaracterizations of nadir antenna patterns and as a means of facilitating improved estimates. The proposed techniques are explored in the context of CYGNSS's 16 nadir antenna patterns, where it is shown that nonuniform gain variability arises when comparing the updated nadir patterns relative to initial estimates. The differences range between −3 and 3 dB, while suggesting peak antenna gains in the range of 14.5–15.5 dB across the individual channels. Particular emphasis as part of the proposed procedures was placed on the ability to decouple physical incidence angle-dependent behavior from antenna gain uncertainties as a result of the geometrical properties of the data taken during rolled periods. Future studies are encouraged to explore other possible information contained in the rolled measurements, e.g., with respect to the reflectivity properties of land surfaces.

Both for zenith (direct signal) and nadir (reflected signal) channel calibration and validation activities, operation in a rolled state for durations as short as 1–7 days is expected to achieve the demonstrated improvement in calibration. Such brief roll maneuvers could be included in the early on-orbit commissioning phase of future mission operations to promote the use of the calibration methods proposed.

The effects of incorporating the updated patterns in terms of promoting enhanced calibration quality of Level-1 observations are explored in the third and final part of this series.

References

[1] C. Ruf et al., *CYGNSS Handbook*, 2nd ed., Ann Arbor, MI, USA: Michigan Publishing Services, 2022.

[2] S. Gleason, M. Al-Khaldi, and D. McKague, "Cyclone global navigation satellite system (CYGNSS): Algorithm theoretical basis document level 1A DDM calibration," Univ. Michigan, Ann Arbor, MI, USA, Tech. Rep. 148-0136, 2023.

[3] S. Gleason, M. Al-Khaldi, and D. McKague, "Cyclone global navigation satellite system (CYGNSS): Algorithm theoretical basis document level 1B DDM calibration," Univ. Michigan, Ann Arbor, MI, USA, Tech. Rep. 148-0137, 2023.

[4] T. Wang, C. S. Ruf, B. Block, D. S. McKague, and S. Gleason, "Design and performance of a GPS constellation power monitor system for improved CYGNSS L1B calibration," *IEEE J. Sel. Topics Appl. Earth Observ. Remote Sens.*, vol. 12, no. 1, pp. 26–36, Jan. 2019, doi: 10.1109/JSTARS.2018.2867773.

[5] T. Wang et al., "Dynamic calibration of GPS effective isotropic radiated power for GNSS-reflectometry Earth remote sensing," *IEEE Trans. Geosci. Remote Sens.*, vol. 60, 2022, Art. no. 5800512, doi: 10.1109/TGRS.2021.3070238.

[6] S. Gleason, M. M. Al-Khaldi, C. S. Ruf, D. S. McKague, T. Wang, and A. Russel, "Characterizing and mitigating digital sampling effects on the CYGNSS level 1 calibration," *IEEE Trans. Geosci. Remote Sens.*, vol. 60, 2022, Art. no. 5802812, doi: 10.1109/TGRS.2021.3120026.

[7] D. Bai, C. S. Ruf, and D. Moller, "Calibration of the polarimetric GNSS-R sensor in the rongowai mission," *IEEE Trans. Geosci. Remote Sens.*, vol. 63, 2025, Art. no. 5801618, doi: 10.1109/TGRS.2025.3558131.

[8] W. Wan et al., "Initial evaluation of the first Chinese GNSS-R mission BuFeng-1 A/B for soil moisture estimation," *IEEE Geosci. Remote Sens. Lett.*, vol. 19, pp. 1–5, Jul. 2022, doi: 10.1109/LGRS.2021.3097003.

[9] F. Huang et al., "Tianmu-1 constellation GNSS-R in-orbit performance: Spatiotemporal characteristics, product applications, and polarimetric features," *IEEE Trans. Geosci. Remote Sens.*, vol. 63, 2025, Art. no. 5802020, doi: 10.1109/TGRS.2025.3581343.

[10] M. M. Al-Khaldi et al., "Utilizing in-orbit CYGNSS roll maneuvers for improved level-1 calibration—Part I: Application to direct signal channels," *IEEE Trans. Geosci. Remote Sens.*, vol. 64, 2026, Art. no. 5801416.

[11] M. M. Al-Khaldi et al., "Utilizing in-orbit CYGNSS roll maneuvers for improved level-1 calibration—Part III: Assessments of nadir observables," *IEEE Trans. Geosci. Remote Sens.*, 2026.

[12] S. Gleason, C. S. Ruf, A. J. O'Brien, and D. S. McKague, "The CYGNSS level 1 calibration algorithm and error analysis based on on-orbit measurements," *IEEE J. Sel. Topics Appl. Earth Observ. Remote Sens.*, vol. 12, no. 1, pp. 37–49, Jan. 2019, doi: 10.1109/JSTARS.2018.2832981.

[13] C. Ruf et al., "Characterization of CYGNSS ocean surface wind speed products," *Remote Sens.*, vol. 16, no. 22, p. 4341, Nov. 2024, doi: 10.3390/rs16224341.

[14] A. M. Warnock, C. S. Ruf, A. Russel, M. M. Al-Khaldi, and R. Balasubramaniam, "CYGNSS level 3 merged wind speed data product for storm force and surrounding environmental winds," *IEEE J. Sel. Topics Appl. Earth Observ. Remote Sens.*, vol. 17, pp. 6189–6200, 2024, doi: 10.1109/JSTARS.2024.3379934.

[15] M. M. Al-Khaldi, A. Bringer, and J. T. Johnson, "Studies of a rapid change detector using CYGNSS level-2 wind speed products," *IEEE J. Sel. Topics Appl. Earth Observ. Remote Sens.*, vol. 14, pp. 7931–7937, 2021, doi: 10.1109/JSTARS.2021.3101500.

[16] J. Park, J. T. Johnson, Y. Yi, and A. J. O'Brien, "Using 'Rapid revisi,' CYGNSS wind speed measurements to detect convective activity," *IEEE J. Sel. Topics Appl. Earth Observ. Remote Sens.*, vol. 12, no. 1, pp. 98–106, Jan. 2019, doi: 10.1109/JSTARS.2018.2848267.

[17] J. Crespo, D. Posselt, and S. Asharaf, "CYGNSS surface heat flux product development," *Remote Sens.*, vol. 11, no. 19, p. 2294, Oct. 2019, doi: 10.3390/rs11192294.

[18] S. Asharaf, B. Guan, and D. E. Waliser, "CYGNSS satellite sampling of surface heat fluxes across atmospheric river life cycles," *Geophys. Res. Lett.*, vol. 52, no. 10, pp. 1–10, May 2025, doi: 10.1029/2024gl113370.

[19] H. X. Bui, E. D. Maloney, E. M. Riley Dellaripa, and B. Singh, "Wind speed, surface flux, and intraseasonal convection coupling from CYGNSS data," *Geophys. Res. Lett.*, vol. 47, no. 21, pp. 1–11, Oct. 2020, doi: 10.1029/2020gl090376.

[20] E. D. Maloney and D. L. Hartmann, "Modulation of eastern north Pacific hurricanes by the Madden–Julian oscillation," *J. Climate*, vol. 13, no. 9, pp. 1451–1460, May 2000, doi: 10.1175/1520-0442(2000)013<1451:MOENPH>2.0.CO;2.

Authorized licensed use limited to: University of Michigan Library. Downloaded on July 22,2026 at 17:42:47 UTC from IEEE Xplore. Restrictions apply.

[21] H. Carreno-Luengo, C. S. Ruf, S. Gleason, and A. Russel, "Capturing soil surface freeze dynamics over the Arctic-Boreal zone with GNSS-reflectometry," *IEEE Trans. Geosci. Remote Sens.*, vol. 63, 2025, Art. no. 5802315, doi: 10.1109/TGRS.2025.3570213.

[22] H. Carreno-Luengo and C. S. Ruf, "Mapping freezing and thawing surface state periods with the CYGNSS based F/T seasonal threshold algorithm," *IEEE J. Sel. Topics Appl. Earth Observ. Remote Sens.*, vol. 15, pp. 9943–9952, 2022, doi: 10.1109/JSTARS.2022.3216463.

[23] L. J. Wernicke, C. C. Chew, and E. E. Small, "Spatially interpolated CYGNSS data improve downscaled 3 km SMAP/CYGNSS soil moisture," *Remote Sens.*, vol. 16, no. 16, p. 2924, Aug. 2024, doi: 10.3390/rs16162924.

[24] O. Eroglu, M. Kurum, D. Boyd, and A. C. Gurbuz, "High spatio-temporal resolution CYGNSS soil moisture estimates using artificial neural networks," *Remote Sens.*, vol. 11, no. 19, p. 2272, Sep. 2019, doi: 10.3390/rs11192272.

[25] M. P. Clarizia, N. Pierdicca, F. Costantini, and N. Floury, "Analysis of CYGNSS data for soil moisture retrieval," *IEEE J. Sel. Topics Appl. Earth Observ. Remote Sens.*, vol. 12, no. 7, pp. 2227–2235, Jul. 2019, doi: 10.1109/JSTARS.2019.2895510.

[26] S. H. Yueh, R. Shah, M. J. Chaubell, A. Hayashi, X. Xu, and A. Colliander, "A semiempirical modeling of soil moisture, vegetation, and surface roughness impact on CYGNSS reflectometry data," *IEEE Trans. Geosci. Remote Sens.*, vol. 60, 2022, Art. no. 5800117, doi: 10.1109/TGRS.2020.3035989.

[27] A. Warnock and C. Ruf, "Response to variations in river flowrate by a spaceborne GNSS-R river width estimator," *Remote Sens.*, vol. 11, no. 20, p. 2450, Oct. 2019, doi: 10.3390/rs11202450.

[28] J. Zhang and Y. J. Morton, "Inland water body surface height retrievals using CYGNSS delay Doppler maps," *IEEE Trans. Geosci. Remote Sens.*, vol. 61, 2023, Art. no. 4209316, doi: 10.1109/TGRS.2023.3330410.

[29] C. Chew, E. Small, and H. Huelsing, "Flooding and inundation maps using interpolated CYGNSS reflectivity observations," *Remote Sens. Environ.*, vol. 293, Aug. 2023, Art. no. 113598, doi: 10.1016/j.rse.2023.113598.

[30] H. Carreno-Luengo, G. Luzi, and M. Crosetto, "Above-ground biomass retrieval over tropical forests: A novel GNSS-R approach with CyGNSS," *Remote Sens.*, vol. 12, no. 9, p. 1368, Apr. 2020, doi: 10.3390/rs12091368.

[31] M. Asgarimehr, D. Entekhabi, and A. Camps, "Diurnal vegetation moisture cycle in the Amazon and response to water stress," *Geophys. Res. Lett.*, vol. 51, no. 19, pp. 1–11, Oct. 2024, doi: 10.1029/2024gl111462.

[32] M. Morris, C. Chew, J. T. Reager, R. Shah, and C. Zuffada, "A novel approach to monitoring wetland dynamics using CYGNSS: Everglades case study," *Remote Sens. Environ.*, vol. 233, Nov. 2019, Art. no. 111417, doi: 10.1016/j.rse.2019.111417.

[33] B. Dong et al., "Underestimation of methane emissions from the sudd wetland: Unraveling the impact of wetland extent dynamics," *Geophys. Res. Lett.*, vol. 51, no. 16, pp. 1–10, Aug. 2024, doi: 10.1029/2024gl110690.

[34] C. Gerlein-Safdi, A. A. Bloom, G. Plant, E. A. Kort, and C. S. Ruf, "Improving representation of tropical wetland methane emissions with CYGNSS inundation maps," *Global Biogeochemical Cycles*, vol. 35, no. 12, pp. 1–14, Dec. 2021, doi: 10.1029/2020gb006890.

[35] A. M. Balakhder, M. M. Al-Khaldi, and J. T. Johnson, "On the coherency of ocean and land surface specular scattering for GNSS-R and signals of opportunity systems," *IEEE Trans. Geosci. Remote Sens.*, vol. 57, no. 12, pp. 10426–10436, Dec. 2019, doi: 10.1109/TGRS.2019.2935257.

[36] M. M. Al-Khaldi, J. T. Johnson, S. Gleason, E. Loria, A. J. O'Brien, and Y. Yi, "An algorithm for detecting coherence in cyclone global navigation satellite system mission level-1 delay-Doppler maps," *IEEE Trans. Geosci. Remote Sens.*, vol. 59, no. 5, pp. 4454–4463, May 2021, doi: 10.1109/TGRS.2020.3009784.

[37] J. T. Johnson, J. V. Toporkov, P. A. Hwang, and J. D. Ouellette, "Efficient calculation of the Kirchhoff integral for predicting the bistatic normalized radar cross section of ocean-like surfaces," *IEEE Trans. Geosci. Remote Sens.*, vol. 61, 2023, Art. no. 2001414.

[38] T. Elfouhaily, B. Chapron, K. Katsaros, and D. Vandemark, "A unified directional spectrum for long and short wind-driven waves," *J. Geophys. Res., Oceans*, vol. 102, no. C7, pp. 15781–15796, Jul. 1997.

[39] P. A. Hwang, D. M. Burrage, D. W. Wang, and J. C. Wesson, "Ocean surface roughness spectrum in high wind condition for microwave backscatter and emission computations," *J. Atmos. Ocean. Technol.*, vol. 30, no. 9, pp. 2168–2188, Sep. 2013.

[40] P. A. Hwang, Y. Fan, F. J. Ocampo-Torres, and H. García-Nava, "Ocean surface wave spectra inside tropical cyclones," *J. Phys. Oceanogr.*, vol. 47, no. 10, pp. 2393–2417, Oct. 2017.

[41] W. J. Pierson and L. Moskowitz, "A proposed spectral form for fully developed wind seas based on the similarity theory of SA Kitaigorodskii," *J. Geophys. Res.*, vol. 69, pp. 5181–5190, Feb. 1964.

[42] M. M. Al-Khaldi, J. T. Johnson, A. J. O'Brien, A. Balenzano, and F. Mattia, "Time-series retrieval of soil moisture using CYGNSS," *IEEE Trans. Geosci. Remote Sens.*, vol. 57, no. 7, pp. 4322–4331, Jul. 2019, doi: 10.1109/TGRS.2018.2890646.

[43] T. Wang, V. U. Zavorotny, J. T. Johnson, C. S. Ruf, and Y. Yi, "Modeling of sea state conditions for improvement of cygnss L2 wind speed retrievals," in *Proc. IEEE Int. Geosci. Remote Sens. Symp.*, Jul. 2018, pp. 8288–8291, doi: 10.1109/IGARSS.2018.8518686.

[44] T. Wang, V. U. Zavorotny, J. Johnson, Y. Yi, and C. Ruf, "Integration of cygnss wind and wave observations with the wavewatch III numerical model," in *Proc. IEEE Int. Geosci. Remote Sens. Symp.*, Jul. 2019, pp. 8350–8353, doi: 10.1109/IGARSS.2019.8900481.

[45] R. K. Pearson, Y. Neuvo, J. Astola, and M. Gabbouj, "Generalized Hampel filters," *EURASIP J. Adv. Signal Process.*, vol. 2016, no. 1, pp. 1–18, Aug. 2016, doi: 10.1186/s13634-016-0383-6.



Mohammad M. Al-Khaldi (Member, IEEE) received the bachelor's degree in electrical engineering from American University of Sharjah, Sharjah, United Arab Emirates, in 2015, the M.S. degree in electrical engineering from Texas A&M University, College Station, TX, USA, in 2017, the M.S. degree in electrical and computer engineering from The Ohio State University, Columbus, OH, USA, in 2019, and the Ph.D. degree from the Department of Electrical and Computer Engineering and the ElectroScience Laboratory, The Ohio State University, in 2020.

He was a Project Scientist I, Post-Doctoral Fellow II, and Post-Doctoral Fellow I at the University Corporation for Atmospheric Research's (UCAR's) COSMIC Program, Boulder, CO, USA. He is currently a Research Scientist at the Department of Electrical and Computer Engineering and the ElectroScience Laboratory, The Ohio State University. His research interests include applied electromagnetics, rough surface scattering, and spaceborne remote sensing.

Dr. Al-Khaldi has been a member of the NASA CYGNSS Mission Science Team, the NASA CYGNSS Mission Calibration and Validation Team, the NASA GNSS Science Team, the IEEE GRSS Technical Committee on Modeling in Remote Sensing, and the IEEE GRSS Technical Committees on Frequency Allocations in Remote Sensing. He has been an Associate Member of the Commissions B and F of the International Union of Radio Science (URSI) and the NASA CSDA GNSS-R Subject Matter Expert (SME). He served as an Associate Editor for *Radio Science* and a Topical Associate Editor for IEEE TRANSACTIONS ON GEOSCIENCE AND REMOTE SENSING.



Scott Gleason (Senior Member, IEEE) received the B.S. degree in electrical and computer engineering from the State University of New York at Buffalo, Buffalo, NY, USA, in 1991, the M.S. degree in engineering from Stanford University, Stanford, CA, USA, in 1999, and the Ph.D. degree in applied physics from the University of Surrey, Surrey, U.K., in 2007.

He is currently the President of Daaxa LLC, Boulder, CO, USA, specializing in GNSS instruments, calibration, and remote sensing applications. He is a Co-Investigator on the science team and Instrument Scientist for the NASA CYGNSS Mission. He has worked in the areas of astronautics, remote sensing and global navigation satellite systems for more than 20 years, including at the NASA Goddard Space Flight Center, Greenbelt, MD, USA; Stanford's GPS Laboratory, Stanford, CA, USA; Surrey Satellite Technology Ltd., Guildford, U.K.; Concordia University, Montreal, QC, Canada; the Southwest Research Institute, San Antonio, TX, USA; the University Corporation for Atmospheric Research, Boulder; and the National Oceanography Centre, Southampton, U.K.

Authorized licensed use limited to: University of Michigan Library. Downloaded on July 22,2026 at 17:42:47 UTC from IEEE Xplore. Restrictions apply.



Christopher S. Ruf (Life Fellow, IEEE) received the B.A. degree in physics from the Reed College, Portland, OR, USA, in 1982, and the Ph.D. degree in electrical and computer engineering from the University of Massachusetts Amherst, Amherst, MA, USA, in 1987.

He was with Intel Corporation, Aloha, OR, USA; Hughes Space and Communication, El Segundo, CA, USA; the NASA Jet Propulsion Laboratory, Pasadena, CA, USA; and Penn State University, University Park, PA, USA. He is currently the Frederick Bartman Collegiate Professor of climate and space science and the Director of the Space Institute, University of Michigan, Ann Arbor, MI, USA, and a Principal Investigator of the NASA CYGNSS Mission. His research interests include remote sensing methods, applications, and technology.

Prof. Ruf is a member of the National Academy of Engineering and American Geophysical Union and a fellow of American Meteorological Society. He is the Vice Chair of the Commission F of U.S. National Committee of the International Radio Science Union. He is the former Editor-in-Chief of IEEE TRANSACTIONS ON GEOSCIENCE AND REMOTE SENSING and has served on the Editorial Board for *Radio Science*, *Journal of Atmospheric and Oceanic Technology*, and *Scientific Reports*.



Joel T. Johnson (Fellow, IEEE) received the bachelor's degree in electrical engineering from Georgia Institute of Technology, Atlanta, GA, USA, in 1991, and the S.M. and Ph.D. degrees from Massachusetts Institute of Technology, Cambridge, MA, USA, in 1993 and 1996, respectively.

He is currently a Professor with the Department of Electrical and Computer Engineering and the ElectroScience Laboratory, The Ohio State University, Columbus, OH, USA. His research interests include microwave remote sensing, propagation, and electromagnetic wave theory.

Dr. Johnson is a member of the Commissions B and F of the International Union of Radio Science (URSI), the Tau Beta Pi, the Eta Kappa Nu, and the Phi Kappa Phi. He received the 1993 Best Paper Award from the IEEE Geoscience and Remote Sensing Society, was named an Office of Naval Research Young Investigator, the National Science Foundation Career Award, the PECASE Award Recipient in 1997, and was recognized by U.S. National Committee of URSI as a Booker Fellow in 2002. He served as the Technical Program Co-Chair for the 2017 International Geoscience and Remote Sensing Symposium. He is the Past Chair of the GRSS Technical Committee on Frequency Allocations in Remote Sensing. He has been an Associate Editor of IEEE TRANSACTIONS ON GEOSCIENCE AND REMOTE SENSING since 2000.



Darren S. McKague (Member, IEEE) received the Ph.D. degree in astrophysical, planetary, and atmospheric sciences from the University of Colorado, Boulder, CO, USA, in 2001.

He was a Systems Engineer with Ball Aerospace, Boulder, and Raytheon, Aurora, CO, USA, and as a Research Scientist at Colorado State University. He is currently an Associate Research Scientist with the Department of Climate and Space Sciences and Engineering, University of Michigan, Ann Arbor, MI, USA. His work has focused on remote sensing with emphasis on the development of space-borne microwave remote sensing hardware, microwave remote sensor calibration techniques, and mathematical inversion techniques for geophysical retrievals. His experience with remote sensing hardware includes systems engineering for several advanced passive and active instrument concepts and the design of the calibration subsystem on the Global Precipitation Mission (GPM) Microwave Imager (GMI), as well as the development of calibration and intercalibration techniques for the GPM constellation. His algorithm experience includes the development of a near-real time algorithm for the joint retrieval of water vapor profiles, temperature profiles, cloud liquid water path, and surface emissivity for the Advanced Microwave Sounding Unit (AMSU), Colorado State University, and the development of the precipitation rate, precipitation type, sea ice, and sea surface wind direction algorithms for the risk reduction phase of the conical scanning microwave imager/sounder (CMIS).



Anthony Russel received the B.S. degree in computer science engineering from Michigan State University, East Lansing, MI, USA, in 2014.

He is currently a member of the Engineering Staff with the Space Physics Research Laboratory, College of Engineering, University of Michigan, Ann Arbor, MI, USA. His primary engineering activities involve algorithm development and large-scale data processing as a member of the Science Operations Center for the CYGNSS Mission.



William L. Wells received the bachelor's degree in aerospace engineering from The University of Texas at Austin, Austin, TX, USA, in 2006.

He is currently a Staff Systems Engineer with the Department of Space Instrumentation, Southwest Research Institute, San Antonio, TX, USA. He has over 17 years of experience spanning all phases of space mission development and execution. His career focus is systems engineering for constellation missions. He is concurrently the Operations Phase Systems Engineering lead for the Cyclone Global Navigation Satellite System (CYGNSS) Mission and the Project Systems Engineer for the Polarimeter to Unify the Corona and Heliosphere (PUNCH) Mission.



Tianlin Wang (Senior Member, IEEE) received the B.E. degree in electrical engineering from East China University of Science and Technology, Shanghai, China, in 2009, the M.S. degree in radio physics from Fudan University, Shanghai, in 2012, and the Ph.D. degree in electrical engineering from the University of Michigan, Ann Arbor, MI, USA, in 2021.

From 2021 to 2023, he was the President's Post-Doctoral Scholar of the Department of Electrical and Computer Engineering and the ElectroScience Laboratory, The Ohio State University, Columbus, OH, USA. He is currently a Research Technologist with the Earth Science Section, Jet Propulsion Laboratory, California Institute of Technology, Pasadena, CA, USA. His research interests include microwave remote sensing, microwave measurements, radio frequency (RF) circuits, and wave propagation and scattering.

Dr. Wang is a member of the Tau Beta Pi, the Eta Kappa Nu, and American Geophysical Union (AGU). He received the 2018 IEEE Mikio Takagi Student Prize, the Outstanding Student Presentation Award from the 2018 AGU Fall Meeting, the 2021 Ernest K. Smith USNC-URSI Student Prize (second place), the Young Scientist Awards from the 44th Photonics and Electromagnetics Research Symposium, and the XXXVth URSI General Assembly and Scientific Symposium in 2023. He currently serves as the Chair for the Modeling in Remote Sensing (MIRS) Technical Committee and the Chapters Committee of the IEEE Geoscience and Remote Sensing Society (GRSS).



Dorina Twigg received the B.S.E. degree in computer engineering from the University of Michigan, Ann Arbor, MI, USA, in 1991, and the M.S. degree in computer science from Wayne State University, Detroit, MI, USA, in 2012.

She is currently a member of the Engineering Staff with the Space Physics Research Laboratory, College of Engineering, University of Michigan, and has a lead role in satellite commanding and scientific data processing with the Science Operations Center for the CYGNSS NASA Earth Venture Mission.

Patrick McEnaney, photograph and biography not available at the time of publication.

Joshua Synowiec, photograph and biography not available at the time of publication.

Authorized licensed use limited to: University of Michigan Library. Downloaded on July 22,2026 at 17:42:47 UTC from IEEE Xplore. Restrictions apply.